

Adjoint Shape Optimization of Hypersonic Blunt Bodies Including the Effect of Graphite Ablation

Oguz K. Onay, Sinan Eyi

Department of Aerospace Engineering, Middle East Technical University, Ankara 06800, Turkey
Corresponding author: okonay@ae.metu.edu.tr

Abstract: One of the aims of the study, is to develop a numerical analysis tool for thermochemical ablation problem under hypersonic flow conditions. The other aim is to include the effects of the graphite ablation to a design optimization tool which uses adjoint method. In this study, IRV2 geometry is selected as the original geometry and optimization study is performed under reacting flow conditions. Drag coefficient of the geometry is reduced without increasing the stagnation point temperature. After the optimization study, ablation behavior of the original geometry and the optimized geometry have been analyzed and compared.

Keywords: Adjoint, Shape Optimization, Hypersonic Flows, Ablation, Reactive Flows.

1 Introduction

Ablation is loss of mass from the surface of materials with the mechanisms like melting, sublimation, erosion or surface chemical reactions. It is a critical phenomenon in aerospace engineering, especially in thermal protection systems of reentry vehicles, rocket nozzle throats and pulsed plasma thrusters. It has also applications in natural and medical sciences; such as the melting problem of glaciers and healing of the tumors. This study deals with only the thermal protection systems of hypersonic vehicles.

Ablation problem is a critical issue in terms of the performance of hypersonic vehicles. Shields should be thick enough to protect the inside of a vehicle and thin enough to reduce the cost and total weight. Besides, local recession may change the geometry and this may affect the aerodynamic characteristics of vehicles. Ablation rates change the properties of the boundary layer. Both the thermal properties and the chemical composition of ablation products directly affect the composition of air surrounds the vehicle.

The design of thermal protection system is a complex phenomenon which includes many disciplines. Using numerical optimization and CFD techniques is one of the feasible options for this purpose. Recently, a design optimization tool is developed for hypersonic conditions by Eyi and Yumuşak [1] using adjoint method. In their study, they have used Lobbs sphere as the base geometry and aimed to reduce the drag of the geometry without increasing the stagnation point temperature. Seager and Agarwal [2] have also studied on a similar problem using multi-objective genetic algorithm. In both of these studies drag and the stagnation point temperatures of the vehicle have been reduced.

In the current study, it is aimed to include the effects of ablation to the design optimization of blunt bodies for chemically reacting hypersonic flows. In the following sections, first the modeling of ablation and flow phenomena is given. Later, design optimization method is explained. Then, results related to ablation modeling have been shown. Drag minimization study of a blunt geometry (IRV2) has been performed. Finally, the ablation behaviors of the original and the optimized geometries have been compared using thermochemical ablation code.

2 Ablation Analysis Approach for Non-charring Material

2.1 In-depth Energy Calculations

One of the most common approaches for the in-depth calculations of ablation problem is to use Landau transformation [3, 4] method for 1-D modeling studies. In Landau transformation approach, the ablating domain is normalized with the instantaneous size of the solution grid. Since the length is normalized, no remeshing is required for the numerical solution but an appropriate advection term has to be attached to the node points as shown in Figure 1. Both advective and diffusive terms require a transformation as shown in Equation (1). In this equation, ρ, C_p, L_n and η_j stand for density, specific heat, instantaneous domain length and normalized coordinates of the 1-D ablating domain. As shown in Figure 1, local advective velocities on the grid nodes are inversely proportional to the distance from ablating surface.

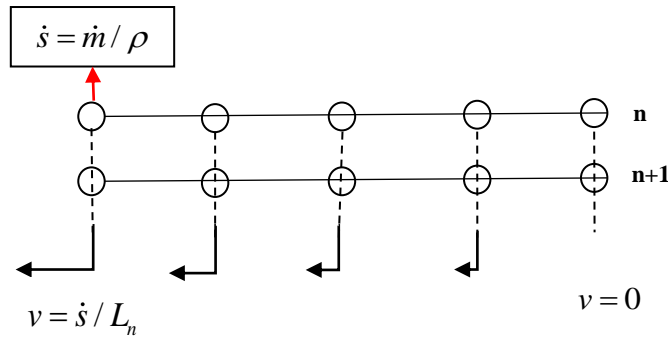


Figure 1: Implementation of Landau transformation [3, 4] for in-depth conduction solution

$$\rho C_p \frac{\partial T}{\partial t} = \frac{1}{L_n^2} \frac{\partial}{\partial \eta} \left(k \frac{\partial T}{\partial \eta} \right) + \frac{1-\eta_j}{L_n} \dot{s} \frac{\partial T}{\partial \eta} \quad (1)$$

One of the future aims of the study is to obtain a basis for a multi-dimensional modeling code. Although, usage of Landau transformation is practical, useful and fast for 1-D solutions, it is not usually easy to obtain a unified approach for the normalization of a multidimensional domain in a curvilinear coordinate system. Hence, remeshing the domain at each time step of a transient solution may be more suitable for multi-dimensional applications. If the numerical grid is reconstructed for each time step, transformation of diffusive and advective terms is not required. The implementation of remeshing with the inclusion of Landau advection term is shown in Figure 2. In remeshing, Equation (1) in Landau transformation can be converted into Equation (2).

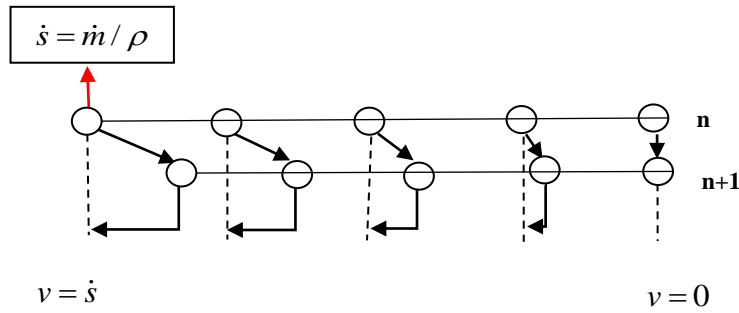


Figure 2: Usage of Landau advection term with remeshing

$$\rho C_p \frac{\partial T}{\partial t} = \frac{\partial}{\partial x} \left(k \frac{\partial T}{\partial x} \right) + \left(1 - \frac{x_j^{n+1}}{L - \int_t^{t+\Delta t} \dot{s} dt} \right) \dot{s} \frac{\partial T}{\partial x} \quad (2)$$

In the current study, a semi-Lagrangian method has also been implemented. If interpolation is used, there is no need for an advective term, and Equation (3) can be used. In this method, a second order piecewise polynomial has been implemented for interpolation. Since, the variable values on the nodes of the new domain are unknown, these values should be obtained from the previous time step values. Thus, appropriate stencil selection is required in order to perform the numerical solution of conduction problem. The usage of interpolation and stencil selection are shown in Figure 3.

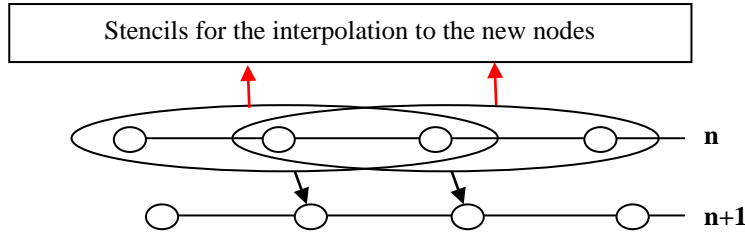


Figure 3: Interpolation with remeshing and stencil selection close to the ablating Edge

$$\rho C_p \frac{\partial T}{\partial t} = \frac{\partial}{\partial x} \left(k \frac{\partial T}{\partial x} \right) \quad (3)$$

All temperature distribution solutions have been obtained using linearized Δ -form temporal discretization as shown below, and solved in the same linear system of the thermochemistry equations given in the next section.

$$\left[I - \Delta t \frac{\partial R}{\partial W} \right] \Delta W = \Delta t R \quad (4)$$

2.2 Surface Thermochemistry Calculations

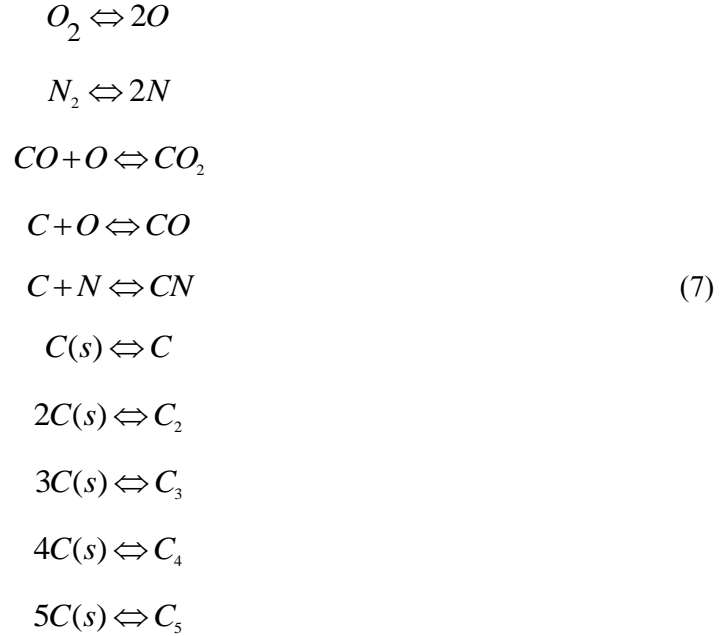
Mass blowing rate parameter (B') is a measure of blowing rate from the ablating surface. It is obtained by nondimensionalization with the mass transfer coefficient and can be defined as shown in Equation (5). It is one of the most critical parameters to be obtained with the surface thermochemistry calculations. Usage of readily-prepared tables for B' as a function of surface temperature and boundary layer edge pressure is a very common approach in equilibrium surface thermochemistry analysis [5, 6, 7]. In this study, to improve the accuracy, the use of interpolation tables is avoided and B' is solved simultaneously with in-depth temperature distribution and species concentrations on the ablating surface.

$$B' = \frac{\dot{m}}{\rho_e u_e C_m} \quad (5)$$

Using the definition of dimensionless blowing rate parameter, mass balance on the ablating surface can be written as in Equation (6). For pure carbon material ablation problem, mass balance can be written using the elemental mass fractions of N, O and C atoms. Left hand side of the equation stands for the elemental concentration on the surface, the first term on the right hand side is the concentration inside the material and the second term is the concentration on the boundary layer edge.

$$(1+B')y_{wk} = B'y_{sk} + y_{ek} \quad (6)$$

Nitridation, oxidation, combination/decomposition and sublimation reactions are given in Equation (7). Except sublimation, these reactions can also be found in Scala and Gilbert [8]. Reactions related to sublimation are given in Palmer and Shelef [9].



Equilibrium constant of the reactions can be written as a function of partial pressures and stoichiometric coefficients of the species as shown;

$$K_p = p_j^{v_j} p_i^{-v_i} \quad (8)$$

Equilibrium constant is also a function of the wall temperature. Thus, the equation to be solved for each reaction becomes;

$$10^a 10^{-b/T} - p_j^{v_j} p_i^{-v_i} = 0 \quad (9)$$

To have equal number of unknowns and equations system can be closed using the following equations. The relations for elemental mass fractions and sum of partial pressures are given in Equation (10) and (11), respectively.

$$y_{wk} = \frac{M_k}{pM_w} \sum_i^N p_i \quad (10)$$

$$p - \sum_i^N p_i = 0 \quad (11)$$

The set of thermochemical equations is solved using Newton iterations as shown;

$$\left[\frac{\partial R}{\partial W} \right] \Delta W = -R \quad (12)$$

2.3 Ablation Calculation Using CFD Analysis Results

This section is about ablation calculation in solid surface if the boundary layer edge condition is known from a CFD solution. Energy balance between the boundary layer edge and the ablating surface should be satisfied. Ablation calculation includes the surface thermochemistry and conduction into the material. If the species concentrations, temperature and the pressure are known at the boundary layer edge, thermochemical ablation can be calculated. Energy balance on the ablating surface is shown in Figure 4.

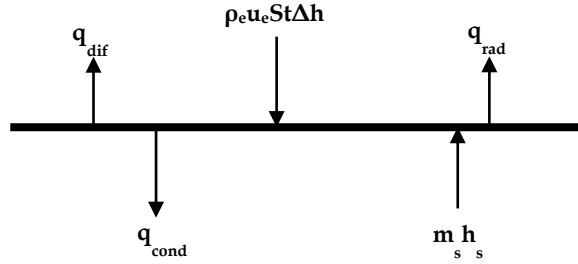


Figure 4: Energy balance on the ablating surface

Equation for energy balance on the ablating surface can be written as shown below for a unity Lewis number assumption ($Le=1$).

$$-k \frac{\partial T}{\partial x} = \rho_e u_e St (h_r - (1+B')h_w) + \dot{m}_s h_s - \sigma \varepsilon T^4 \quad (13)$$

Besides, it is assumed that the boundary layer edge composition is not affected by the ablation products. Also, only C atoms are included in the ablating material. Thus, elemental mass balance relations can be reduced as shown;

$$y_{sC} = 1, y_{eC} = 0, y_{sO} = 0, y_{sN} = 0 \quad (14)$$

$$\begin{aligned} (1+B') y_{wO} &= y_{eO} \\ (1+B') y_{wC} &= B' \\ (1+B') y_{wN} &= y_{eN} \end{aligned} \quad (15)$$

CFD analysis result on the boundary layer edge becomes the boundary condition of ablation analysis for an uncoupled study as shown in Figure 5.

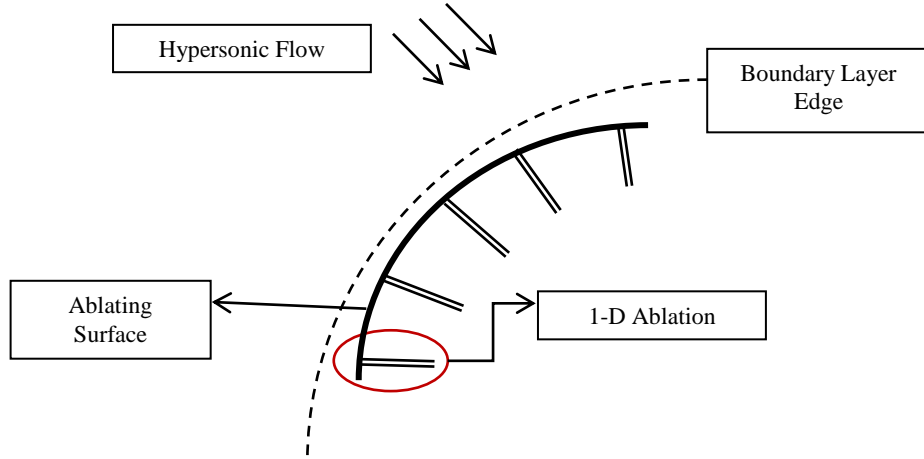


Figure 5: Ablation calculation using CFD analysis results

Another requirement for an uncoupled ablation calculation is the heat transfer coefficient approximation. Heat transfer coefficient should be calculated simultaneously with the ablation analysis, since, this coefficient is a function of wall temperature. Heat transfer rate can be calculated with the relation that is used by Zoby et al [10]. Information about the adiabatic wall enthalpy can be obtained from the CFD results using adiabatic wall boundary condition on the vehicle surface.

$$\dot{q}_w = \text{Re}_\theta^{-1} \left(\frac{\rho^*}{\rho} \right) \left(\frac{\mu^*}{\mu} \right) \rho_e u_e (h_{aw} - h_w) \text{Pr}_w^{-0.6} \quad (16)$$

Reference density, ρ^* , and viscosity, μ^* , should be evaluated at a reference temperature which is defined by Eckert [11].

$$T^* = 0.5T_w + 0.22T_{aw} + 0.28T_e \quad (17)$$

Using heat transfer rate approximation, unblown heat transfer coefficient can be calculated as in equation below;

$$\rho_e u_e St_0 = \frac{\dot{q}_w}{(h_r - h_w)} \quad (18)$$

Since, the relation above is defined for a non-ablating wall, blowing correction should be applied to the heat transfer coefficient as given;

$$\frac{St}{St_0} = \frac{\ln(1+B')}{B'} \quad (19)$$

3 CFD Analysis and Design Optimization Approach

3.1 Flow Simulation Approach

Axisymmetric Navier-Stokes equations have been used in order to model the hypersonic flow around the blunt body. Non-dimensional form of axisymmetric Navier-Stokes equations in generalized coordinates can be written as shown below.

$$\frac{\partial \hat{F}(\hat{W})}{\partial \xi} + \frac{\partial \hat{G}(\hat{W})}{\partial \eta} + \frac{\partial \hat{F}_v(\hat{W})}{\partial \xi} + \frac{\partial \hat{G}_v(\hat{W})}{\partial \eta} + \hat{H} + \hat{H}_v - \hat{S} = 0 \quad (20)$$

In the equation above, ξ and η represent the generalized curvilinear coordinates of the numerical domain, \hat{W} is the conservative vector, \hat{F} , \hat{G} are the inviscid flux vectors in ξ and η directions, \hat{F}_v and \hat{G}_v represent the viscous flux vectors in the same directions. Similarly, \hat{H} , \hat{H}_v are the inviscid and viscous axisymmetric source vectors and \hat{S} is the source vector related to species production.

$$\hat{W} = \frac{1}{J} \begin{bmatrix} \rho \\ \rho u \\ \rho v \\ \rho e_t \\ \rho_1 \\ \vdots \\ \rho_{K-1} \end{bmatrix} \quad \hat{F} = \frac{1}{J} \begin{bmatrix} \rho U \\ \rho u U + \xi_x p \\ \rho v U + \xi_y p \\ (\rho e_t + p)U \\ \rho_1 U \\ \vdots \\ \rho_{K-1} U \end{bmatrix} \quad \hat{G} = \frac{1}{J} \begin{bmatrix} \rho V \\ \rho u V + \eta_x p \\ \rho v V + \eta_y p \\ (\rho e_t + p)V \\ \rho_1 V \\ \vdots \\ \rho_{K-1} V \end{bmatrix} \quad (21)$$

$$\hat{F}_v = \frac{1}{J \text{Re}} \begin{bmatrix} 0 \\ \xi_x \tau_{xx} + \xi_y \tau_{xy} \\ \xi_x \tau_{xy} + \xi_y \tau_{yy} \\ \xi_x \beta_x + \xi_y \beta_y \\ 0 \\ \vdots \\ 0 \end{bmatrix} \quad \hat{G}_v = \frac{1}{J \text{Re}} \begin{bmatrix} 0 \\ \eta_x \tau_{xx} + \eta_y \tau_{xy} \\ \eta_x \tau_{xy} + \eta_y \tau_{yy} \\ \eta_x \beta_x + \eta_y \beta_y \\ 0 \\ \vdots \\ 0 \end{bmatrix} \quad (22)$$

$$\hat{H} = \frac{1}{yJ} \begin{bmatrix} \rho v \\ \rho uv \\ \rho v^2 \\ (\rho e_t + p)v \\ \rho_1 v \\ \vdots \\ \rho_{K-1} v \end{bmatrix} \quad \hat{H}_v = \frac{1}{yJ \text{Re}} \begin{bmatrix} 0 \\ \tau_{xy} \\ \tau_{yy} - \tau_{\theta\theta} \\ \beta_y \\ 0 \\ \vdots \\ 0 \end{bmatrix} \quad \hat{S} = \frac{1}{J} \begin{bmatrix} 0 \\ 0 \\ 0 \\ 0 \\ \dot{\omega}_1 \\ \vdots \\ \dot{\omega}_{K-1} \end{bmatrix} \quad (23)$$

$$\beta_x = u\tau_{xx} + v\tau_{xy} - q_x \quad \beta_y = u\tau_{xy} + v\tau_{yy} - q_y \quad (24)$$

Shear stress terms in the viscous flux vectors can be defined as shown below;

$$\tau_{xx} = \mu \left(\frac{4}{3} \frac{\partial u}{\partial x} - \frac{2}{3} \frac{\partial v}{\partial x} \right) \quad \tau_{xy} = \mu \left(\frac{\partial u}{\partial y} + \frac{\partial v}{\partial x} \right)$$

$$\tau_{yy} = \mu \left(\frac{4}{3} \frac{\partial v}{\partial y} - \frac{2}{3} \frac{\partial u}{\partial x} \right) \quad \tau_{\theta\theta} = -\frac{2}{3} \mu \left(\frac{\partial u}{\partial x} + \frac{\partial v}{\partial y} \right) + \frac{4}{3} \mu \frac{v}{y} \quad (25)$$

Cell centered finite volume approach is used for the numerical analysis. Upwind flux splitting is implemented for the inviscid flux vectors. F^+ , F^- , G^+ and G^- are calculated using Van Leer method [12] as shown below.

$$\begin{aligned} \hat{F}_{i\pm 1/2,j} &= \hat{F}_{i\pm 1/2,j}^+ (\hat{W}_{i\pm 1/2,j}^-) + \hat{F}_{i\pm 1/2,j}^- (\hat{W}_{i\pm 1/2,j}^+) \\ \hat{G}_{i,j\pm 1/2} &= \hat{G}_{i,j\pm 1/2}^+ (\hat{W}_{i,j\pm 1/2}^-) + \hat{G}_{i,j\pm 1/2}^- (\hat{W}_{i,j\pm 1/2}^+) \end{aligned} \quad (26)$$

MUSCL (Monotonic Upstream-Centered Scheme Conservation Law) [12] interpolation is implemented for higher order discretizations.

$$\begin{aligned} \hat{W}_{i+1/2}^- &= \hat{W}_i + \left\{ \frac{\phi}{4} [(1-\kappa)\nabla + (1+\kappa)\Delta] \right\}_i \\ \hat{W}_{i+1/2}^+ &= \hat{W}_{i+1} - \left\{ \frac{\phi}{4} [(1+\kappa)\nabla + (1-\kappa)\Delta] \right\}_{i+1} \end{aligned} \quad (27)$$

If a limiter function is not used, MUSCL scheme causes undesirable oscillations in the regions where high gradients in flow variables exist. Van Albada limiter [13] is used in order to avoid these oscillations and this function is defined as shown below.

$$\phi(r) = \frac{r + r^2}{1 + r^2} \quad (28)$$

$$r_i = \frac{\Delta_i + \epsilon}{\nabla_i + \epsilon} \quad (29)$$

At relatively high temperatures, thermodynamic properties become the function of temperature. In the flow solution, specific heat of each species is set to be the fourth order polynomial of temperature as shown below. Similarly the enthalpy and the entropy of each species have been calculated using polynomial functions of the temperature.

$$\frac{C_{pk}}{R} = a_{1,k} \frac{1}{T^4} + a_{2,k} \frac{1}{T^3} + a_{3,k} \frac{1}{T^2} + a_{4,k} \frac{1}{T} + a_{5,k} + a_{6,k} T + a_{7,k} T^2 + a_{8,k} T^3 + a_{9,k} T^4 \quad (30)$$

Specific heat and the enthalpy of the mixture can be calculated as shown below using the densities of each species. The coefficient values of the polynomial functions are taken from JANAF Tables [14].

$$C_p = \sum_{k=1}^K \frac{\rho_k}{\rho} C_{pk} \quad (31)$$

$$h = \sum_{k=1}^K \frac{\rho_k}{\rho} h_k \quad (32)$$

Free stream air consists of mostly N_2 and O_2 . Flow is assumed to be 5 species composition

including N, O, NO, N₂ and O₂. Although, the ionization of N and O atoms take place for temperatures higher than 9000 K, ionizations have been excluded from the numerical analysis. The chemical reactions have been modeled for I number of reactions and K number of species as in Equation (33).

$$\sum_{k=1}^K \nu'_{k,i} \chi_k \Leftrightarrow \sum_{k=1}^K \nu''_{k,i} \chi_k \quad (33)$$

In the equation above $\nu'_{k,i}$ and $\nu''_{k,i}$ stand for the stoichiometric coefficients and χ_k stands for the chemical symbol of the k^{th} species. The forward reaction rates can be defined as Arrhenius type relations where A_i is the pre-exponential factor and E_i is the activation energy.

$$k_{fi} = A_i T^{\beta_i} \exp\left(\frac{-E_i}{R_u T}\right) \quad (34)$$

3.2 Design Optimization Approach

Optimization problem can be defined as below where the function F_i is an objective function to be minimized and G_j is a constraint function. In the functions given, W , X , D , I and J stand for state of variables, grid coordinates, design variables, number of design variables and number of constraint functions.

$$F_i[\hat{W}(D_i), X(D_i), D_i], \quad (i=1, \dots, I) \quad (35)$$

$$G_j[\hat{W}(D_i), X(D_i), D_i], \quad (j=1, \dots, J) \quad (36)$$

In gradient base optimization, the search direction should be usable and feasible. The sensitivities should be calculated. Sensitivities are the derivatives of the objective and constraint functions with respect to design variables. Both direct differentiation and adjoint methods can be used for the analytical sensitivity calculations. If the direct differentiation method is used, the differentiation can be implemented using Equation (37).

$$\frac{dF}{dD_i} = \frac{\partial F}{\partial \hat{W}} \left(\frac{d\hat{W}}{dD_i} \right) + \frac{\partial F}{\partial X} \left(\frac{dX}{dD_i} \right) + \frac{\partial F}{\partial D_i} \quad (37)$$

A sensitivity code can be developed by taking the derivatives of the discretized residual equations with respect to design variables. Discretized form of the flow equations can be written in the form below.

$$\hat{R}(\hat{W}(D_i), X(D_i), D_i) = 0 \quad (38)$$

Differentiating the discretized form of the residual equations analytically results in the equation below;

$$\left[\frac{\partial \hat{R}}{\partial \hat{W}} \right] \left(\frac{d\hat{W}}{dD_i} \right) + \left[\frac{\partial \hat{R}}{\partial X} \right] \left(\frac{dX}{dD_i} \right) + \frac{\partial \hat{R}}{\partial D_i} = 0 \quad (39)$$

Equation can be rearranged in order to calculate the flow variable sensitivities.

$$\left[\frac{\partial \hat{R}}{\partial \hat{W}} \right] \left(\frac{d\hat{W}}{dD_i} \right) = - \left[\frac{\partial \hat{R}}{\partial X} \right] \left(\frac{dX}{dD_i} \right) - \frac{\partial \hat{R}}{\partial D_i} \quad (40)$$

If the optimization problem has larger number of design variables than the number of constraint functions, adjoint method has more advantages. In this method, discretized flow equations are considered as constraint functions. If the Equation (39) is multiplied by Lagrange multipliers and summed up with the Equation (37) the following equation can be obtained.

$$\frac{dF}{dD_i} = \frac{\partial F}{\partial X} \left(\frac{dX}{dD_i} \right) + \frac{\partial F}{\partial D_i} + \Lambda^T \left\{ \left[\frac{\partial \hat{R}}{\partial X} \left(\frac{dX}{dD_i} \right) + \frac{\partial \hat{R}}{\partial D_i} \right] \right\} + \underbrace{\left\{ \left[\frac{\partial \hat{R}}{\partial \hat{W}} \right]^T \Lambda + \left(\frac{\partial F}{\partial \hat{W}} \right)^T \right\}}_{\text{chose as zero}} \left(\frac{d\hat{W}}{dD_i} \right) \quad (41)$$

If the last parenthesis on the right hand side is set to be 0, the sensitivities of the objective function can be calculated using the equation below.

$$\frac{dF}{dD_i} = \frac{\partial F}{\partial X} \left(\frac{dX}{dD_i} \right) + \frac{\partial F}{\partial D_i} + \Lambda^T \left\{ \left[\frac{\partial \hat{R}}{\partial X} \left(\frac{dX}{dD_i} \right) + \frac{\partial \hat{R}}{\partial D_i} \right] \right\} \quad (42)$$

The linear system of equations should be solved for the calculation of Lagrange multipliers as given.

$$\left[\frac{\partial \hat{R}}{\partial \hat{W}} \right]^T \Lambda = - \frac{\partial F}{\partial \hat{W}} \quad (43)$$

4 1-D Ablation Calculation Results

4.1 Example In-depth Energy Calculation

In this part of the study, an example solution for the 1-D conduction with recession is represented. It is assumed that the material ablates at a constant wall temperature and the recession rate is constant. The relations that define the problem are given as (44), (45) and (46).

$$\rho C_p \frac{\partial T}{\partial t} = \frac{\partial}{\partial x} \left(k \frac{\partial T}{\partial x} \right) + v \frac{\partial T}{\partial x} \quad (44)$$

$$v = (1 - X_j) \frac{\partial s}{\partial t} \quad (45)$$

$$T_w = T_{abl} \quad x = 0 \quad (46)$$

The problem is defined for a semi-infinite domain. Obviously, it is not possible to define a semi-infinite domain for a numerical solution. Thus, a relatively long and finite domain is used and adiabatic boundary condition is applied implicitly on the rear edge. The analytical solution of the problem is as shown below [5, 6]. The problem becomes steady, if the ablating surface of the domain is set to be the origin of the domain during whole process, and the analytical solution becomes as given.

$$\frac{T(x) - T_i}{T_{abl} - T_i} = e^{-\frac{ds}{dt} \frac{x}{\alpha}} \quad (47)$$

The comparison of analytical solution and the numerical solution for the temperature distribution inside the material at different instants is shown below in Figure 6.

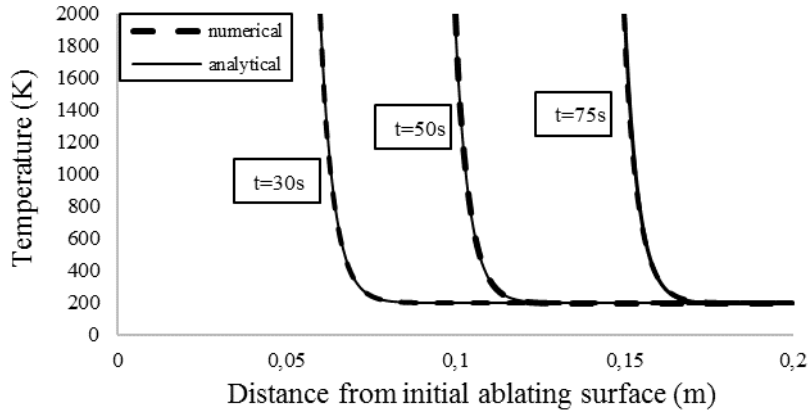


Figure 6: Comparison of analytical and numerical results for temperature distribution – Previously known recession velocity and constant ablation temperature

4.2 Example Surface Thermochemistry Calculations

The blowing rate parameter calculation results of graphite ablation is given in figure 7 for different temperature and pressure values. The boundary layer edge condition is assumed to be $y_O / y_N = 0.3068$ for the obtained B' values at each point.

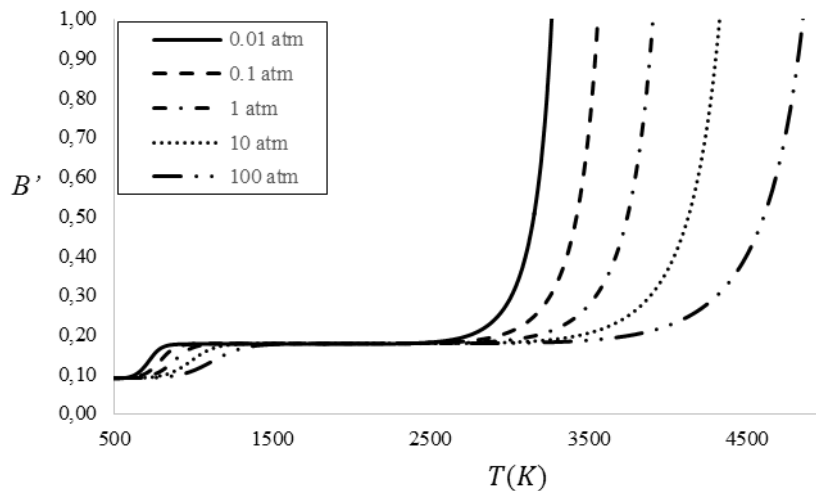


Figure 7: calculated B' values using Newton's method

Also, calculated partial pressure values of species for 1 atm boundary layer edge pressure is given in Figure 8 as an example. These results have been obtained via setting the wall temperature and the stagnation pressure as the known values of the sparse linear systems. Having the boundary layer edge information makes it possible to have an implicit 1-D non-charring equilibrium ablation solver, and the boundary layer edge information should be obtained from the hypersonic flow analysis results.

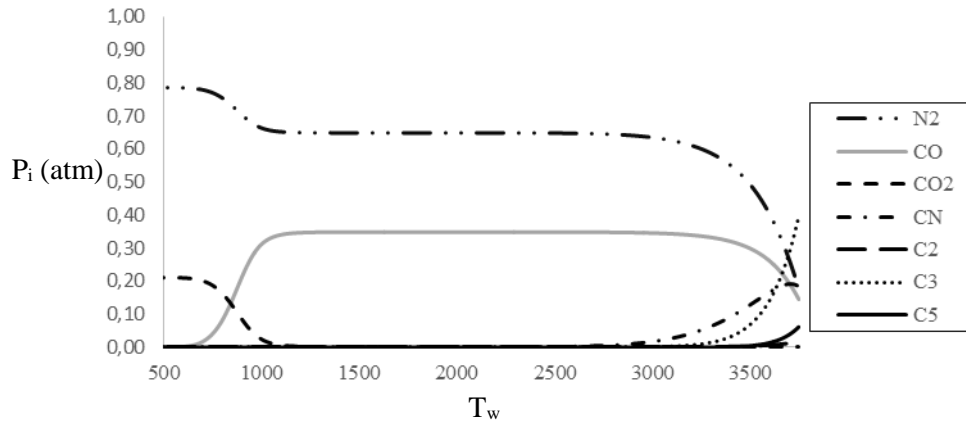


Figure 8: Partial pressures of species on ablating wall at 1 atm boundary layer edge pressure

Below in figure 9, residual histories of equilibrium problem for a single point solution (4000 K and 1 atm) are given for different initialization cases. For each of the cases quadratic convergence of Newton iterations can be seen clearly. In the first initialization case the solution takes about 70 iterations which is a relatively big number for Newton's method. Obtaining the single point solutions via marching the temperature value and initializing the problem with a previously solved temperature results, decreases the number of iterations. Solving the problem with an initialization using the results of 3900 K reduces the number of iterations about to 60 and initializing the problem with the solution of 3950 K reduces the number of iterations up to 10. All three cases and the solution of the problem at 4000 K and 1 atm are shown in table 1.

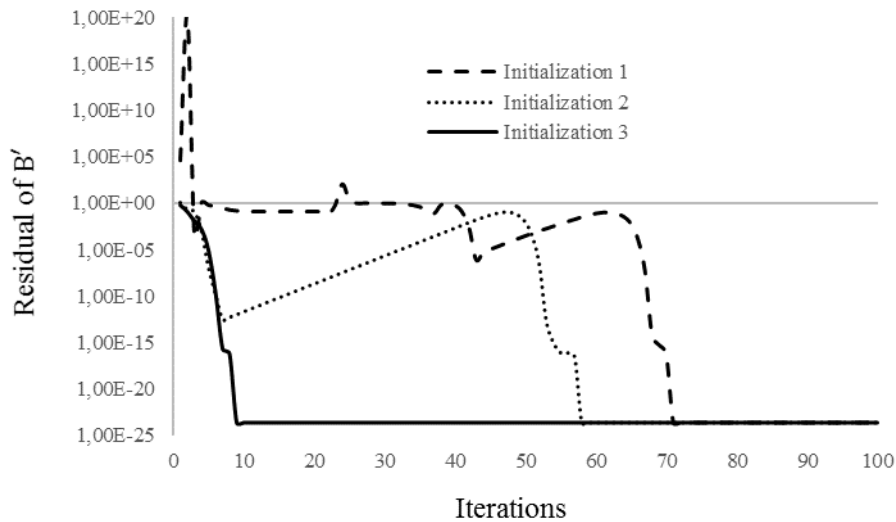


Figure 9: Residual histories of equilibrium solution for different initializations – Solution for $p_e=1 \text{ atm}$, $T_e=4000 \text{ K}$

Table 1: Different initialization cases for equilibrium solution (Boundary Layer Edge Properties: 4000 K and 1 atm)

Initialization 1	Initialization 2 (Initialized with Solution of 3900 K)	Initialization 3 (Initialized with Solution of 3950 K)	Solution for 4000 K
$y_{wO}=0.1000$	$y_{wO}=0.1191$	$y_{wO}=0.1020$	$y_{wO}=8.2105 \times 10^{-2}$
$y_{wC}=0.1000$	$y_{wC}=0.4925$	$y_{wC}=0.5653$	$y_{wC}=0.6502$
$y_{wN}=0.1000$	$y_{wN}=0.3883$	$y_{wN}=0.3326$	$y_{wN}=0.2676$
$B'=0.1000$	$B'=0.9705$	$B'=1.3007$	$B'=1.8593$
$M_w=30.0000$	$M_w=28.1992$	$M_w=28.5235$	$M_w=28.9963$

4.3 Transient Ablation Calculations for Known Boundary Layer Edge Properties

Transient ablation of carbon/carbon material is solved including the conduction into the material using both Landau advection term and interpolation methods. It is assumed that the boundary layer edge conditions are known. Edge properties that have been used as the boundary conditions of the 1-D ablation problem is shown in Table 2. Besides, equilibrium composition for the known edge properties are calculated and shown in Table 3. Initial temperature for the material is assumed to be 1500 K and transient results for mass blowing rate and the wall temperature are shown in Figures 10 and 11.

Table 2: Boundary layer edge properties

T_e	5500 K
$\rho_e u_e St$	3 kg/m ² /s
p_e	0.5 atm
Edge Composition Enthalpy	12392 kJ/kg
Edge Total Enthalpy	15000

Table 3: Mass fraction of equilibrium air species on the edge of the boundary layer for 5500 K and 0.5 atm

O_2	0.00033
O	0.34801
N_2	0.54136
N	0.10099
NO	0.00931

The results obtained with Landau advection and interpolation (semi-Lagrangian method) are highly coherent. The effect of limitation of wall temperature by an ablative material is obvious in Figure 10. Although the boundary layer edge temperature is set to be 5500 K, wall temperature cannot exceed 3500 K. Also, both blowing rate and wall temperature values converges to certain numbers with time. Thus, it is possible to use a transient conduction solution for an ablation problem with a steady state assumption.

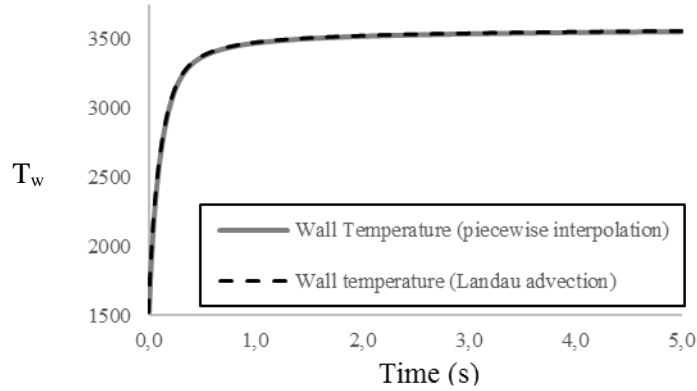


Figure 10: Variation of wall temperature with time using Landau advection and piecewise interpolation

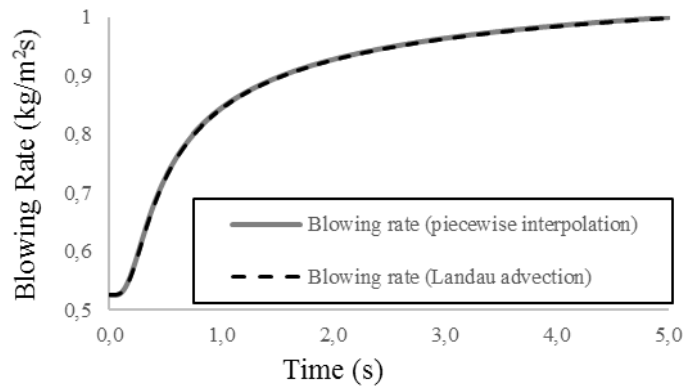


Figure 11: Variation of mass blowing rate with time using Landau advection and piecewise interpolation

5 CFD and Ablation Analysis Results for IRV2 Geometry

IRV2 vehicle geometry with nose radius of 1.95 cm is selected as the base geometry for the CFD analysis, drag optimization and initial ablation analysis studies. Ablation modeling study has already been performed for this geometry and compared with the experimental results by Bianchi et al [15]. Also, Chen and Milos compared finite rate and equilibrium approaches for the similar geometry [16]. Free stream conditions of the case are listed in Table 4.

Table 4: Free stream conditions used for the ablation analysis study on IRV2 geometry [15],[16]

V_∞	5354 m/s
ρ_∞	0.003 kg/m ³
T_∞	1428 K
O	0.2573
N	0.1212
NO	0.0046
N_2	0.6169
O_2	0.0000

Numerical grid used for CFD analysis is shown below in Figure 12 and CFD analysis results are shown in Figure 13 for Mach number, pressure and temperature distributions, and in Figure 14 for atomic N and atomic O concentration distributions in order. Boundary layer edge properties are

extracted from the results during post-processing, in order to be set as the boundary conditions of the ablation analysis study.

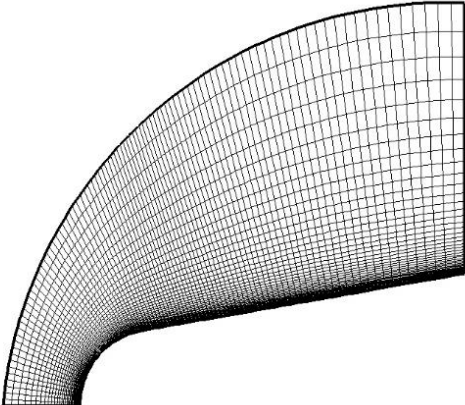


Figure 12: Numerical grid used for CFD analysis - IRV2 geometry

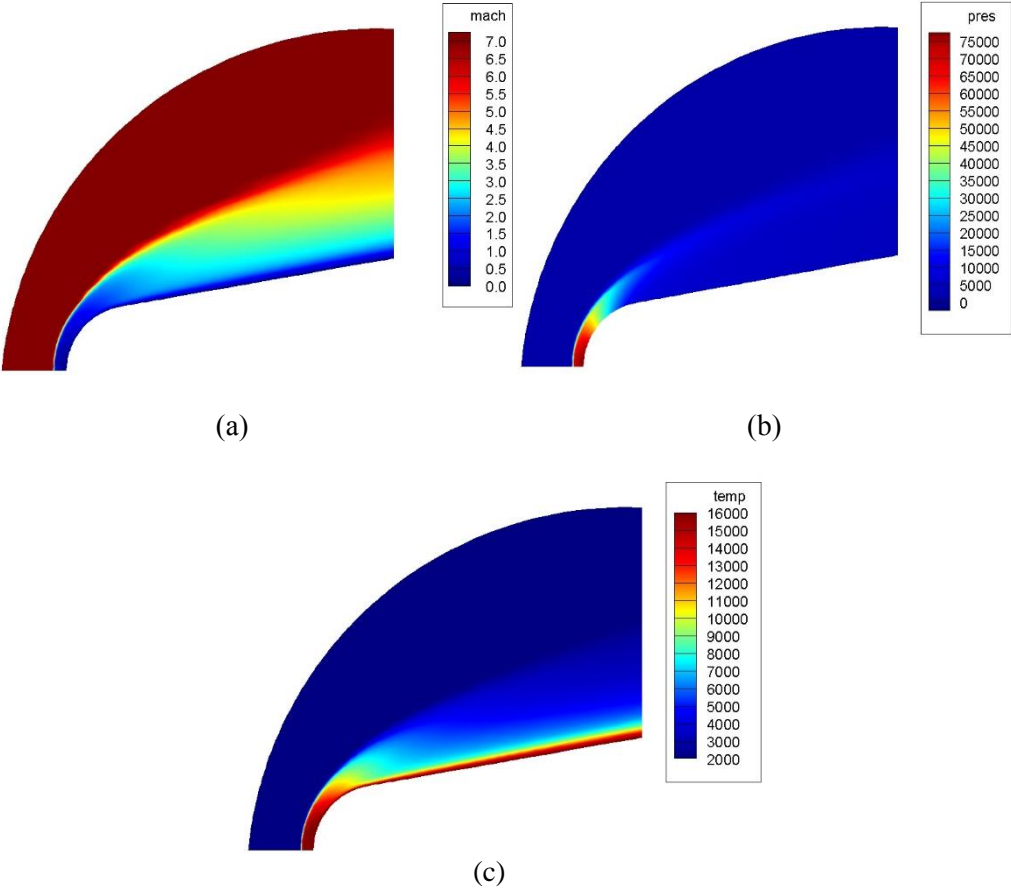


Figure 13: CFD analysis results for IRV2 geometry (a) Mach number (b) pressure-Pascal (c) temperature-Kelvin

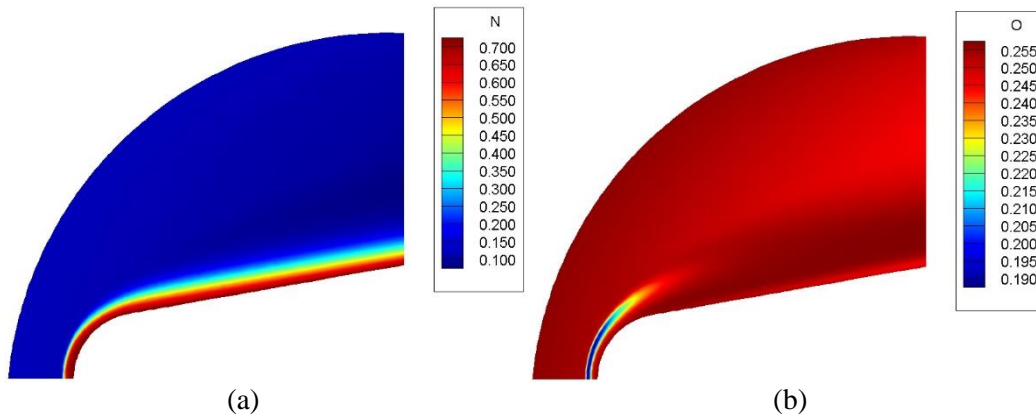


Figure 14: CFD analysis results (a) atomic oxygen mass fraction (b) atomic nitrogen mass fraction

Adiabatic wall properties of CFD solution have been used for the Stanton number approximation which is explained through equations (16)-(19). Ablating wall temperature is iterated between implicit ablation code and Stanton number approximation.

Ablation analysis results for mass blowing rate and wall temperature distribution are shown below in Figure 15 and 16, and compared with experimental data from references [15] and [16]. It can be seen that results have not been calculated at a small region close to the stagnation point since; the heat transfer coefficient approximation is not valid on this point anymore. The mass blowing rate calculation result is coherent with experimental data close to 45° point which is at about 0.015 m distance from the stagnation point. Besides it is seen that wall temperature calculation is satisfactory on the spherical nose surface but the calculation error increases while going far from the stagnation point and on the 10° inclined wall surface.

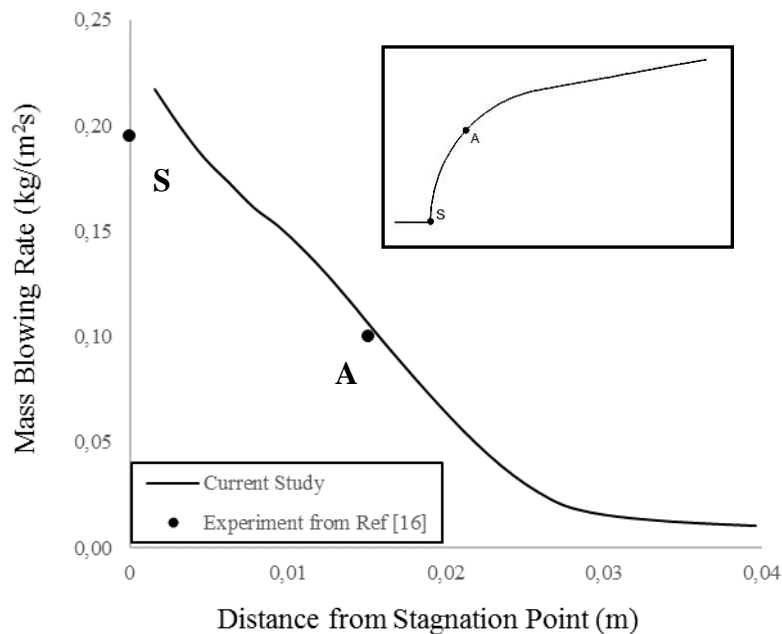


Figure 15: Ablation analysis results - mass blowing rate distribution over the IRV2 nose

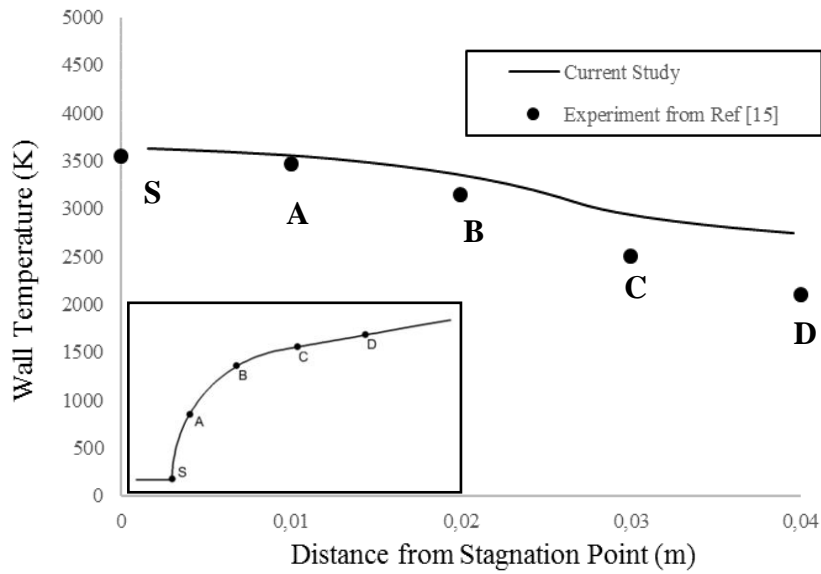


Figure 16: Ablation analysis results – wall temperature distribution over the IRV2 nose

6 Change in the Ablation Behavior of Drag Optimized Geometry

In this part of the study, behavior change for a drag optimized nose [14] is inspected. IRV2 geometry is used as the base geometry. Adjoint method and Bezier-Bernstein polynomials are used for design optimization. Study is performed using 4-6 and 8 design variables (control points) and it is observed that the resulting geometry converges to a specific shape with increasing number of control points. 15.4% improvement is obtained for 4 design points, 15.8% improvement is obtained for 6 design points and 15.9% improvement of drag coefficient is obtained for 8 design points. Comparison of resulting geometries is shown below in Figure 17 for 4, 6 and 8 design points.

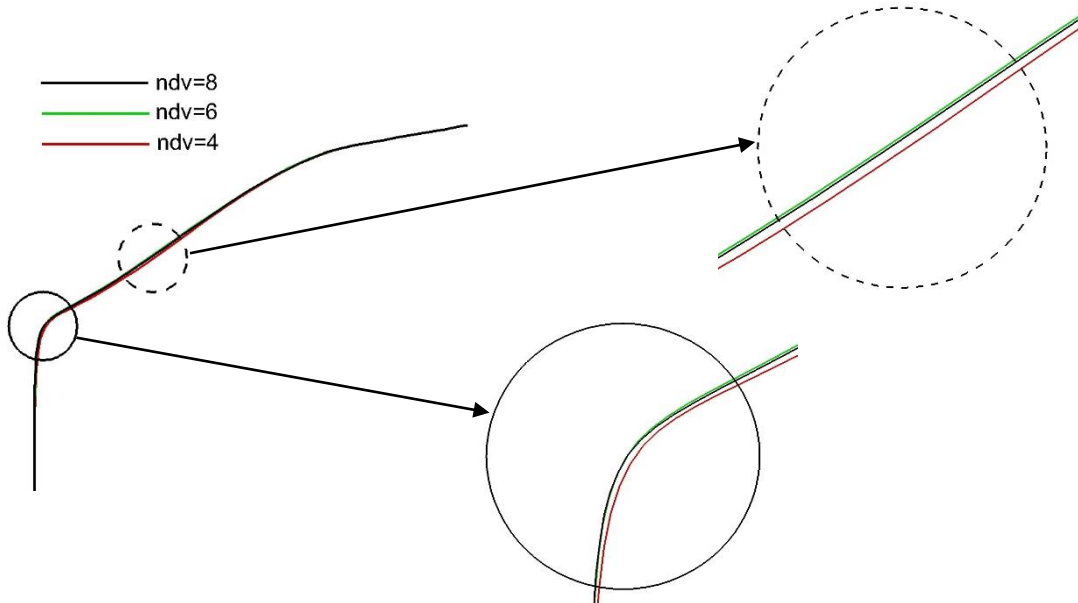


Figure 17: Comparison of drag optimized geometries for 4, 6 and 8 design variables

CFD analysis results for the drag optimized geometry of 8 design variables are shown in Figure 18 (a), (b) and (c) for Mach number, pressure and temperature in order. Besides atomic N and O mass fraction distributions are shown in Figure 19 (a) and (b).

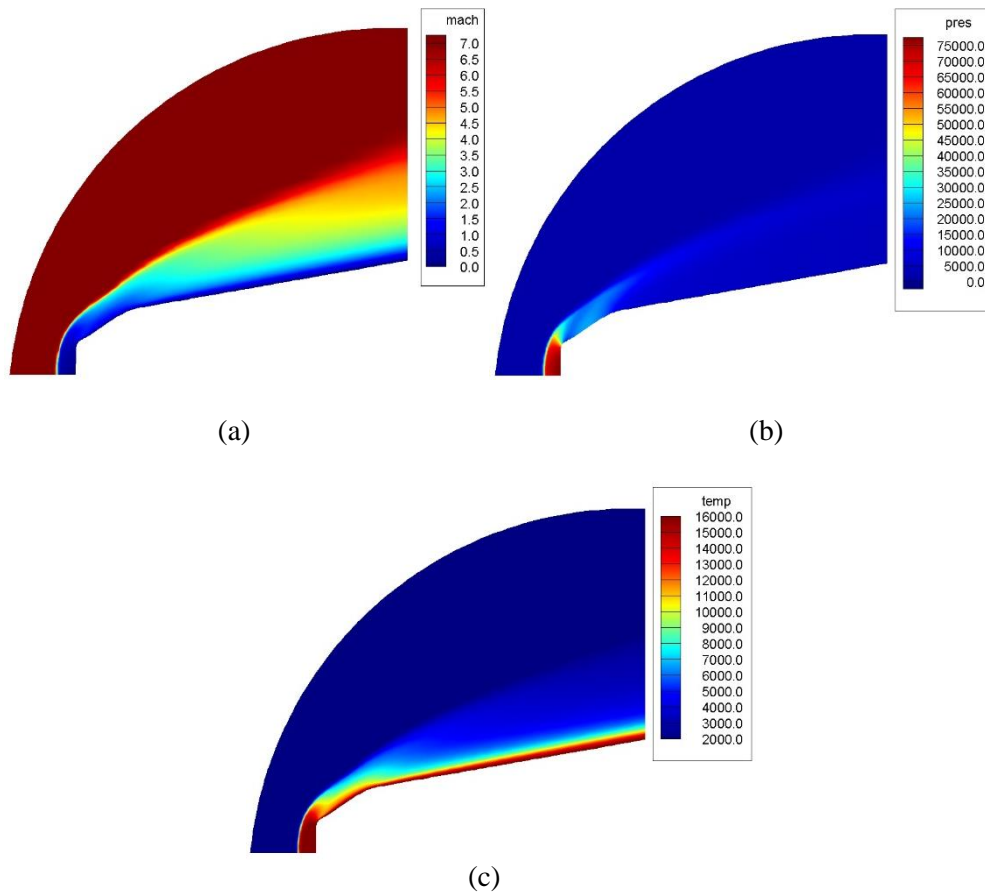


Figure 18: CFD analysis results for drag optimized geometry (a) Mach number (b) pressure-Pascal (c) temperature-Kelvin

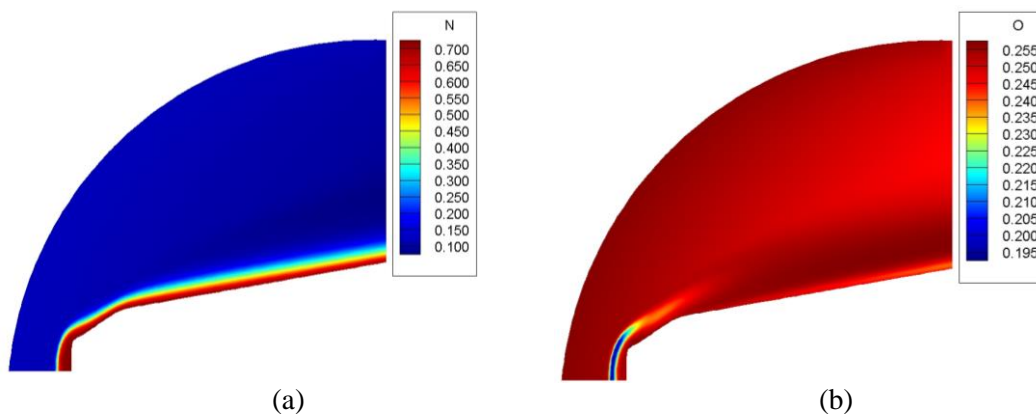
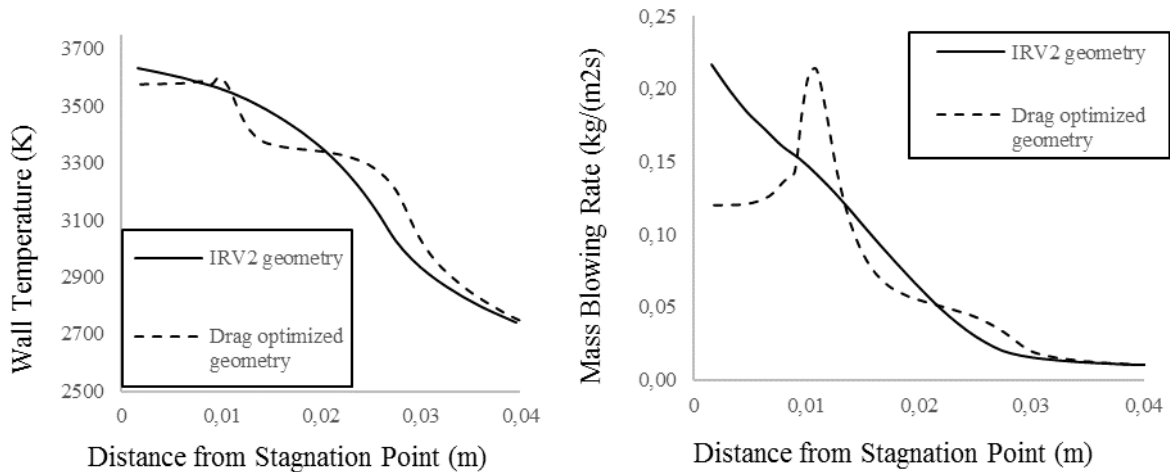


Figure 19: CFD analysis results (a) atomic oxygen mass fraction (b) atomic nitrogen mass fraction for drag optimized geometry

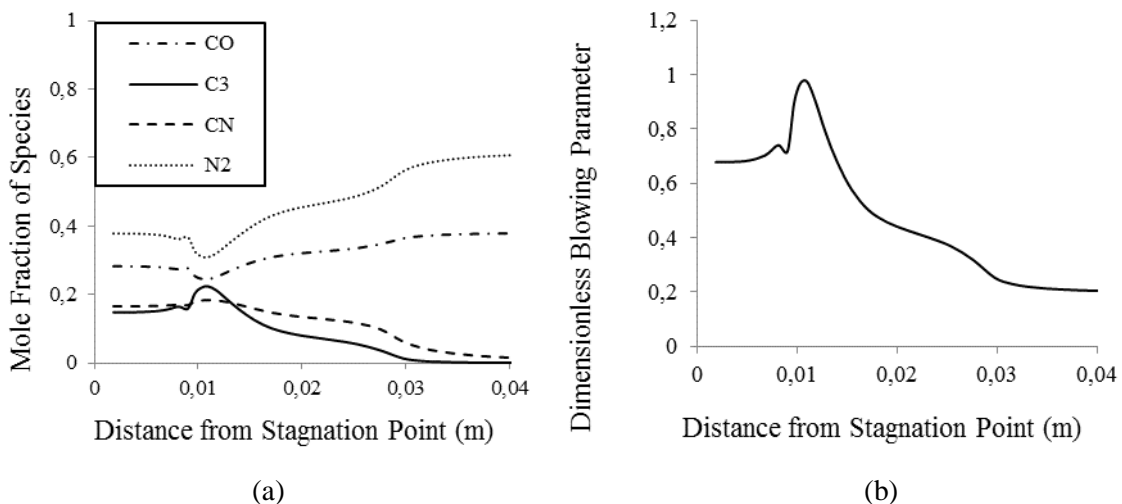
Comparison of mass blowing rate and temperature distributions on the surfaces of IRV2 geometry and drag optimized geometry are given in Figure 20 (a) and (b). Stagnation point temperature on the

designed geometry with and without ablating surface is lower compared to the original geometry. But, low stagnation point temperature does not guarantee a lowered wall temperature distribution on the new geometry. Although, the mass blowing rate is decreased on a flattened nose, sudden pressure decrease on the shoulder of the optimized geometry results in high blowing rates. On the drag optimized geometry, mass blowing rate and B' value at the shoulder are approximately 40 and 30 % higher compared to that of at stagnation point. Besides, shoulder of the new geometry yields almost equal blowing rate value with the stagnation point blowing rate of original IRV2 geometry.

Distribution of dominant species and the B' distribution on the ablating surface are shown in Figure 21 (a) and (b) in order. Sudden change in the distribution character of the species beginning with the shoulder point and the sudden increase in the C_3 concentration on this point can be clearly seen in Figure 21 (a).



(a) (b)
Figure 20: Ablation analysis results (a) mass blowing rate (b) wall temperature distribution on the ablating wall of drag optimized geometry



(a) (b)
Figure 21: Distribution of (a) dominant species (b) B' value on the ablating wall of drag optimized geometry

6 Conclusion

In this study, the modeling of 1-D thermochemical ablation of non-charring materials have been studied. The boundary conditions for ablation analysis are evaluated using a CFD code. The CFD code is based on axisymmetric Navier-Stokes and finite rate chemical reaction equations. A design optimization study has been performed and, the ablation behaviors of the initial and optimized geometries have been compared. The results show that, although the optimized geometry reduces drag and stagnation temperature, whole temperature distribution may not be reduced on the ablating wall. This phenomenon can be explained as follows. Drag coefficient minimization with an adiabatic wall, converges to a geometry with a relatively sharp shoulder and causes an expansion region after the shoulder. Sudden drop of the pressure in the boundary layer causes increase of sublimation and a wall temperature peak. Such peaks on an ablative wall might cause drastic shape and aerodynamic behavior changes under hypersonic conditions. To overcome this problem, another objective function can be defined related to the mass blowing rate and/or wall temperature distribution for an ablating wall.

References

- [1] Eyi, S., Yumuşak, M., "Aerothermodynamic shape optimization of hypersonic blunt bodies", *Engineering Optimization*, Vol. No. 7., pp. 909-926, 2015.
- [2] Seager, J., Agarwal, R.,K., "Hypersonic Blunt-Body Shape Optimization for Reducing Drag and Heat Transfer", *Journal of Thermophysics and Heat Transfer*, 2015.
- [3] Landau, H. G., "Heat Conduction in a Melting Solid," *Quarterly of Applied Mathematics*, Vol. 8, No. 1 , pp. 81-94, 1950.
- [4] Blackwell, B. F., Hogan R. E., "One-Dimensional Ablation Using Landau Transformation and Finite Control Volume Procedure", *Journal of Thermophysics and Heat Transfer*, Vol. 8, No. 2. pp. 282-287, 1994.
- [5] Amar, A. J., Blackwell, B. F., Edwards, J. R., Beerman A. F., "One-Dimensional Ablation Using a Full Newton's Method and Finite Control Volume Procedure", *Journal of Thermophysics and Heat Transfer*, Vol. 22, No. 1, 2008. pp. 71-82.
- [6] Bianchi, D., "Modeling of ablation phenomena in space applications", Ph.D. Thesis, Università degli Studi di Roma "La Sapienza", 2007.
- [7] Milos, F. S., Rasky, D. J., "Review of Numerical Procedures for Computational Surface Thermochemistry", *Journal of Thermophysics and Heat Transfer*, Vol 8, No. 1, pp. 24-32., 1994.
- [8] Scala, S. M., Gilbert, L. M. "Sublimation of Graphite at Hypersonic Speeds", *AIAA Journal*, Vol. 3, No. 9, pp. 1635-1644, 1965.
- [9] Palmer, H.B. and Shelef, M., "Vaporization of Carbon" *Chemistry and Physics of Carbon*, Vol. 4, edited by P.L. Walker, Jr., Marcel Dekker, Inc., New York, 1968.
- [10] Zoby, E. V., Moss, J., N., Suttont K., "Approximate Convective-Heating Equations for Hypersonic Flows", *Journal of Spacecraft*, Vol. 18, No. 1, . pp. 64-70, 1980.
- [11] Eckert, E.R.G., "Survey on Heat Transfer at High Speeds", U.S. Air Force, ARL 189, 1961.
- [12] Van Leer, B., "Towards the ultimate conservative difference scheme, V. a second order sequel to Godunov's method", *Journal of Computational Physics*, Vol. 32, 1979.
- [13] Van Albada, G., Van Leer, B. and Roberts, W. W., "A comparative study of computational methods in cosmic gas dynamics", *Astronomy and Astrophysics*, Vol. 108, pp. 76-84, 1982.
- [14] JANAF Thermochemical Tables, NBS-NSRDS, 37, 1971.
- [15] Bianchi, D., Nasuti, F., Martelli E., "Navier–Stokes Simulations of Hypersonic Flows with Coupled Graphite Ablation", *Journal of Spacecraft and Rockets*, Vol. 47, No. 4., pp. 554-562, 2010.

- [16] Milos, F. S., Chen, Y. K., “Navier–Stokes Solutions with Finite Rate Ablation for Planetary Mission Earth Reentries”, *Journal of Spacecraft and Rockets*, Vol. 42, No. 6, 2005. pp. 961-970.